RESEARCH ARTICLE

Scale-up of an unsteady flow field for enhanced spatial and temporal resolution of PIV measurements: application to leaflet wake flow in a mechanical heart valve

Alessandro Bellofiore · Eilis M. Donohue ·
Nathan J. Quinlan

Abstract A scale-up approach is developed to enhance effective spatial and temporal resolution of PIV measurements. An analysis shows that complete similarity can be maintained for certain unsteady flows and that all types of error in PIV are either reduced or unaffected by scale-up. Implementation and results are described for flow through a mechanical heart valve (MHV), in which high resolution is necessary to advance understanding of the effects of small-scale flow structure on blood cells. With a large-scale model geometry and a low-viscosity model fluid, spatial and temporal resolutions are increased by factors of 5.8 and 118, respectively, yielding the finest resolution to date for MHV flow. Measurements near the downstream tip of a valve leaflet detect eddies as small as 400 μm shed in the leaflet wake. Impulsively started flow exhibits vortex shedding frequencies broadly consistent with the literature on flat-plate and aerofoil wakes, while the physiological unsteady flow waveform promotes 40% higher frequency at peak flow.

1 Introduction

The spatial resolution of particle image velocimetry (PIV) is limited by the requirement for a multi-pixel interrogation window to generate each velocity datum, and temporal resolution is usually limited by camera frame rate and laser repetition rate. These are significant limitations for applications in which small domains or small flow structures are of vital interest. The objective of this work is to enhance the resolution of PIV, without modification to the PIV apparatus itself, by building a scaled-up model of the flow field for one such application in biomedical fluid dynamics.

The application of interest is blood flow through a mechanical heart valve (MHV), a device whose clinical performance is sensitive to small-scale flow, because disease responses are initiated by flow-induced loading of blood cells. Red blood cells measure 8 μm in diameter and 2.6 μm in maximum thickness and account for 40–50% of blood volume, with the remainder comprising liquid plasma and a small volume of other cell types (Fung 1993). The most popular MHV design for several decades has been the bileaflet valve (Fig. 1), most often implanted near the root (inlet) of the aorta (a large blood vessel of approximately circular cross-section). Each leaflet rotates freely to open and close under fluid loading. For an aortic valve under normal conditions, the peak Reynolds number based on diameter is around 6,000 and the valve cycles with a period of around 0.86 s.

MHVs are clinically successful, but they induce abnormal fluid dynamic regimes which result in increased incidence of haemolysis (red blood cell rupture) and thrombosis (blood clotting) in patients who have undergone heart valve replacement (Yoganathan et al. 1992). Although bioprosthetic and polymeric valves provide a closer approximation to physiological flow conditions, mechanical valves are preferred in at least 50% of implantations, especially for young- and middle-aged patients, due to their superior durability (Kidane et al. 2009). It has been demonstrated that prolonged exposure of cells to abnormally high-shear stress is responsible for both haemolysis (Leverett et al. 1972; Paul et al. 2003) and platelet activation (Kroll et al. 1996). Activated

A. Bellofiore · E. M. Donohue · N. J. Quinlan
National Centre for Biomedical Engineering Science,
National University of Ireland, Galway, Galway, Ireland

A. Bellofiore (✉) · E. M. Donohue · N. J. Quinlan
Department of Mechanical and Biomedical Engineering,
National University of Ireland, Galway, Galway, Ireland
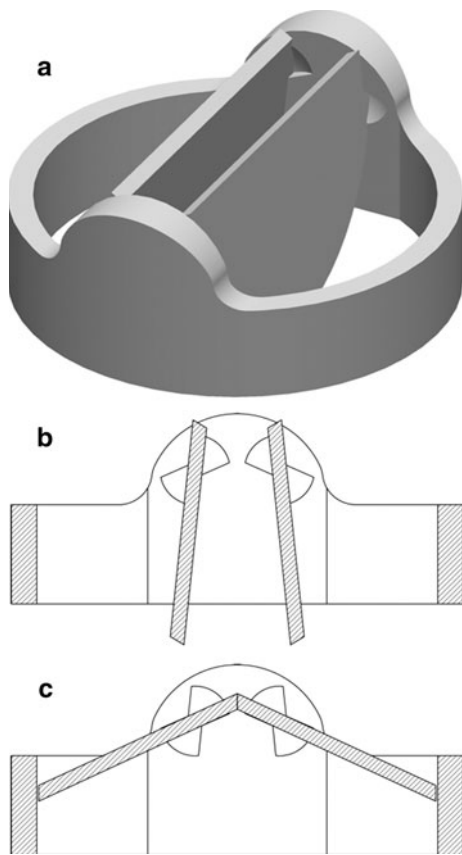e-mail: alessandro.bellofiore@nuigalway.ie

Fig. 1 Sketch of a mechanical heart valve: **a** three-dimensional view and mid-plane section view in **b** fully open and **c** closed position

platelets aggregate to form thrombi (clots) if they become entrapped in zones of low-velocity separated flow (Figliola and Mueller 1981) or recirculating flow (Yoganathan et al. 1978), such as vortices shed downstream of the valve (Bluestein et al. 2000). Therefore, the major goal of MHV research is to develop enhanced valve designs so that the improved fluid dynamic regime may eliminate the need for lifelong anticoagulant therapy (Gott et al. 2003; Dasi et al. 2009).

Mechanically induced blood damage (haemolysis and thrombosis) is initiated by the action of the flow on individual cells. Flow downstream of the valve is often characterised as turbulent, but the pulsatile nature of flow and the range of Reynolds number values indicate that the flow should be considered disturbed or transitional (Yellin 1966; Sutera and Joist 1992). Experiments in steady mean flow have shown that haemolysis levels are significantly higher in turbulent flow than in laminar flow at the same mean shear stress (Kameneva et al. 2004). It is not clear whether the flow is truly turbulent, but it is well established that rapidly varying small flow structures occur downstream of the valve. It has been argued (Ellis et al. 1998; Liu et al. 2000) that the most damaging mechanical effects on blood cells are due to flow structures at scales near cellular size, based on the hypothesis that large eddies simply transport cells

without harmful deformation of their membrane. However, analytical and numerical models have shown that greater cell loading may occur in the more energetic mid-range flow structures (Quinlan and Dooley 2007; Dooley and Quinlan 2009). Hence, knowledge of the blood flow field at small scales is crucial for understanding of the link between non-physiological fluid dynamics and blood damage. Several authors (Baldwin et al. 1994; Ellis et al. 1998; Liu et al. 2000) have estimated the smallest eddy scales in MHV flow by applying the Kolmogorov theory for isotropic, homogeneous and statistically stationary turbulence, which represent questionable assumptions for the short-duration flow under investigation. Reynolds stress, calculated from macroscopic pointwise velocity measurements, has also been proposed as a predictor of blood damage, but its relevance has been questioned on theoretical (Quinlan and Dooley 2007) and experimental (Ge et al. 2008) grounds. In particular, the Reynolds stress provides no information about the length scale of eddies. As a result, direct measurement of the flow field at the small scales seems to be the only reliable approach to gain a well-grounded comprehension of mechanically induced blood damage.

In the open position, a MHV leaflet is a flat semi-elliptical plate immersed in blood flow at a small angle of attack. It is well known that, even at low angle of attack (as in the case of fully open valve), the boundary layer on the suction surface of a wing can undergo separation due to the adverse pressure gradient (Lissaman 1983). In the case of blood flow past valve leaflets, the Reynolds number based on leaflet chord is 3,240 at peak flow. These conditions can be compared with some studies conducted on inclined airfoils at Reynolds number on the order of 10^3 (Huang et al. 2001; Taira and Colonius 2009; Alam et al. 2010), which predict that the free shear layer fails to reattach to the wing surface and survives beyond the trailing edge, thus forming a large wake.

Particle Image Velocimetry (PIV) has been used extensively in the in vitro measurement of the flow of homogeneous, non-cellular blood analogue fluids in MHV designs (Lim et al. 1998; Balducci et al. 2004; Dasi et al. 2007; Kaminsky et al. 2007; Yagi et al. 2009). The finest spatial resolution (defined as the distance between measured velocity vectors) reported to date for field measurement of flow in MHVs is 135-μm vector spacing with 50% overlap of interrogation windows (Ge et al. 2008). The temporal resolution of most MHV PIV studies (15 Hz) represents a coarse sample rate for the heartbeat period of 0.86 s. Higher time resolution (3,000 Hz) has been achieved using a high-speed PIV system (Kaminsky et al. 2008), but with poorer spatial resolution (1,200 μm). There is a need for still higher temporal and spatial resolution in PIV of flow through MHVs to enable direct visualisation and identification of the smallest structures which may interact with cells. The current goal, therefore, is to

measure flow in a homogeneous blood analogue fluid at resolution an order of magnitude greater than cell diameter. This is the smallest scale at which a homogeneous fluid can be considered physically relevant as a model for blood, but measurements at this scale will provide insight into the mechanical environment experienced by blood cells.

Given the importance of small-scale structure in the biomechanical function of devices such as MHVs, the use of a scaled-up experiment is attractive as a means to enhance spatial and temporal resolution of advanced measurement techniques. However, there are only a small number of MHV fluid dynamics studies to date to feature a scaled-up model heart valve. Scaled-up model valve studies have focussed on flow in the hinge region (Healy et al. 1998; Gao et al. 1999), leaflet dynamics (Zhao et al. 2001), near-wall region (Kelly et al. 1999) and cavitation (Chahine 1996). Flow has been investigated in 10:1 scale models by Affeld et al. (1989) with largely qualitative results and in 3:1 models by Knoch et al. (1988) for steady flow. No research to date has combined current PIV methods with a scale-up approach to maximise resolution of measurements in the main valve flow under realistic unsteady conditions.

The aim of the present work is to develop a large-scale whole-valve model that ensures complete dynamic similarity with the full-scale valve, while providing optical access for high-resolution quantitative measurement and visualisation (by PIV) throughout the flow field. This development will facilitate a probing of the small-scale flow structures in the turbulent and/or transitional flow regimes. Following the vast majority of published research on cardiovascular device biomechanics, we model the blood as a homogeneous Newtonian liquid, ignoring the presence of suspended cells. This assumption must be revisited in future research if clear evidence emerges for the existence of flow structures near cellular scale. At the present time, however, there is scope to enhance understanding of MHV operation by characterising the flow at a scale one order of magnitude above cellular scale.

Dimensional analysis of the scale-up approach is presented in Sect. 2. Model design and measurement methods are described in Sect. 3, with an emphasis on the impact of scale-up on the PIV technique and in particular on measurement accuracy. Representative results are presented in Sect. 4 for flow near the downstream tip of the valve leaflet and in its wake. Results are discussed in Sect. 5, with a particular focus on vortex shedding and the analogy with flow over inclined plates and wings.

2 Dimensional analysis

A dimensional analysis of the experimental variables was performed to identify the dimensionless numbers that

must be preserved to obtain dynamic similarity in the scaled-up experiment. We consider a valve consisting of one or more rigid leaflets which are free to rotate about a single axis and is immersed in a periodic flow-field characterised by a reference velocity U (defined here as the spatial mean of axial velocity at peak flow) and frequency f (reciprocal of the heartbeat period). Equation 1 defines the form of the functional dependence of local fluid velocity, u, on the other variables in the experiment. In addition to U, f, spatial coordinates x, y, z and time t, the independent variables are the density of the working fluid ρ, the diameter of the valve D, the dynamic viscosity μ, the mass moment of inertia I of the leaflet, the moment B about the axis of rotation due to weight and buoyancy, and the friction torque F due to the rotation of the leaflet on its hinge.

$$u = u(x, y, z, t, \rho, \mu, D, f, U, I, B, F) \qquad (1)$$

With 3 basic dimensions and 13 variables, 10 dimensionless Π-groups result according to the Buckingham Pi theorem. They are defined in Eq. 2.

$$\frac{u}{U} = g\left(\frac{x}{D}, \frac{y}{D}, \frac{z}{D}, tf, \frac{\rho U D}{\mu}, D\left(\frac{2\pi f \rho}{\mu}\right)^{\frac{1}{2}}, \frac{I}{\rho D^5}, \frac{B}{U^2 \rho D^3}, \frac{F}{\rho U^2 D^3}\right)$$
$$= g(x^*, y^*, z^*, t^*, \mathrm{Re}, \alpha, I^*, B^*, F^*) \qquad (2)$$

The arguments of the function g in Eq. 2, aside from the dimensionless coordinates and time, are the dimensionless numbers that must be preserved in order to obtain experimental similarity between a physiological-scale experiment and the scaled-up experiment. They are the Reynolds number Re and Womersley number α, and the non-dimensionalised mass moment of inertia I^*, weight moment B^* and friction torque F^*, respectively.

Preservation of the Reynolds number requires that

$$\frac{U'}{U} = \frac{\rho}{\rho'} \frac{D}{D'} \frac{\mu'}{\mu} \qquad (3)$$

where primed variables are those in the scaled-up model. The requirements to preserve Womersley number, non-dimensionalised moment of inertia and non-dimensionalised weight moment lead to the following scaling relations.

$$\frac{f'}{f} = \left(\frac{D}{D'}\right)^2 \frac{\mu'}{\mu} \qquad (4)$$

$$\frac{I'}{I} = \frac{\rho'}{\rho}\left(\frac{D'}{D}\right)^5 \qquad (5)$$

$$\frac{B'}{B} = \frac{\rho}{\rho'}\left(\frac{\mu'}{\mu}\right)^2 \frac{D'}{D} \qquad (6)$$

Solid-on-solid friction forces affect the dynamics of the leaflets and, in turn, the development of the flow field.

Friction forces arise between the pivot of the leaflet and the hinge in the valve housing. The precise form of the friction forces is unknown and depends on lubrication of the hinge mechanism by the fluid. For the purposes of discussion, a simple Coulomb friction law is assumed. The contribution of friction is proportional to the net force acting on the leaflet, resulting from the balance of weight and buoyancy:

$$F = \varphi(\rho_S - \rho)gV_L r \qquad (7)$$

where φ is an effective coefficient of friction, ρ_S is fluid density, g is acceleration due to gravity, V_L is the volume of the leaflet (which scales with D^3) and r is the effective moment arm of the friction force about the axis of rotation (which scales with D). Preservation of the dimensionless friction torque $F*$ requires that

$$\frac{\varphi'}{\varphi} = \frac{\rho'}{\rho} \frac{(\rho_S - \rho)}{(\rho'_S - \rho')} \frac{D}{D'} \frac{U'^2}{U^2} \qquad (8)$$

Thus, the requirement for complete similarity imposes Eqs. 3–6 and 8 as constraints on the design of the scaled-up experiment. After the geometric scaling ratio D'/D has been chosen as required to enhance spatial measurement resolution, U′, μ', f and the composition of the leaflet can be chosen to satisfy Eqs. 3–5. (Since the viscosity of available test liquids varies over a much larger range than the density, viscosity is considered to be the primary criterion determining the choice of fluid. For practical purposes, $\rho \cong \rho'$, and so density is not considered an independent design variable.)

It is possible in some circumstances to satisfy both Eqs. 5 and 6 (inertia and buoyancy) by suitable choice of leaflet density and mass distribution. However, in the model described in this paper, the axis of rotation of the leaflets was oriented vertically, so that the effects of buoyancy and weight on leaflet dynamics are eliminated. (This orientation may arise for an implanted valve in a supine patient). Thus, Eq. 6 need not be enforced.

Under some conditions, it may be possible to satisfy Eq. 8 for friction scaling by choosing an appropriate ρ'_S, while still satisfying Eq. 5 for moment of inertia. Conservatively, assuming $\varphi = 1$ for illustrative purposes, the value of $F*$— the order of magnitude of the ratio of hydrodynamic to frictional torque—is around 500. The true value of this ratio is likely to be much larger, since the hinge mechanism is lubricated. This suggests that hinge friction effects are negligible in valve dynamics. Therefore, rather than satisfying Eq. 8 exactly, a practical approach is to ensure that frictional torque is negligible in comparison with hydrodynamic torque in the scaled-up model. This design criterion may be assisted by small changes to the mechanical design of the hinge, if necessary.

This analysis shows that it is possible to replicate exactly the Reynolds number, Womersley number and inertia effects in a scaled-up model mechanical heart valve. This conclusion is applicable to any unsteady flow of an incompressible Newtonian fluid involving rigid bodies with low friction, buoyancy and weight effects, and one degree of freedom each.

3 Apparatus and methods

The experimental flow simulator is designed to provide an in vitro testing environment for a scaled-up model of a bileaflet heart valve, representative of the widely used St. Jude Medical design. In common with many investigations of MHV flow, the experiment is not designed to model a patient-specific anatomical geometry. Rather, the apparatus is designed to replicate the major generic features of flow in a prosthetic heart valve in the aortic position. This allows the creation of standardisable and reproducible flow conditions in the model. The approach also clarifies the interpretation of the results and minimises concern that flow features may be due to specific features of the valve or anatomical geometry.

The model valve is scaled geometrically by a factor of 5.8. This factor was chosen to give a substantial enhancement in measurement spatial resolution, subject to practical constraints due to the size of the associated test section and flow loop. Water was chosen as the blood analogue fluid, giving $\mu'/\mu = 0.29$ and hence, $f'/f = 0.00849$ according to Eq. 4, equivalent to a slowing of the unsteady flow cycle (and increase in effective temporal resolution) by a factor of 118. The low viscosity of water contributes to this effective temporal resolution increase and is the main reason for the choice of fluid. Most of the test section and valve are made in polymethyl methacrylate (PMMA) for optical access. Many optical experimental models of blood flow involve a thick-walled transparent model with planar outer surfaces and the required internal geometry, with a blood analogue fluid chosen to match the refractive index of the model; in the present work, a thin-walled model is used with a fluid of low refractive index. These basic scaling decisions have some implications for the mechanics and optics of the apparatus, which are discussed later in the context of detailed design.

The apparatus, sketched in Fig. 2, comprises a test section housing the model valve, a fluid reservoir, and a computer-controlled piston pump, which provides the required flow conditions for all the experiments.

3.1 Design of the large-scale model valve

The scaled-up valve design is loosely based on the geometry of a St. Jude Medical™ bileaflet mechanical valve
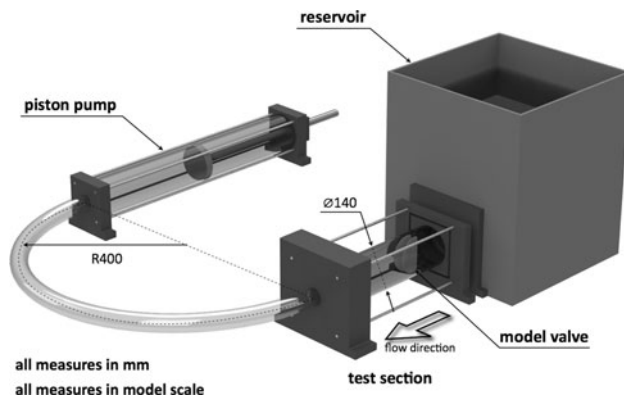
Fig. 2 Schematic diagram of the test apparatus

with orifice diameter of 24 mm. The model valve has two semi-elliptical leaflets, each with two rectangular protrusions which sit in a butterfly-shaped hinge recess. The butterfly constrains the leaflet between closed and fully open positions, as sketched in Fig. 1. The valve orifice has an inner diameter of 140 mm, and the scaled-up leaflets are 5.0 mm thick, giving a scaling factor of approximately 5.8. The assembly of leaflets and hinge blocks is sketched in Fig. 3.

The dimensionless mass moment of inertia of the leaflet and the friction force at the hinges should be preserved to achieve complete similarity between both the physiological-scale and scaled-up leaflets, as discussed in Sect. 2. MHV leaflets are usually made from pyrolytic carbon, which has a density of around 2,190 kg/m^3, while the scaled-up leaflet is made from PMMA with a density of 1,170 kg/m^3, for enhanced optical access and ease of manufacture. The moment of inertia of the model leaflets is adjusted by incorporating stainless steel ballast discs in the
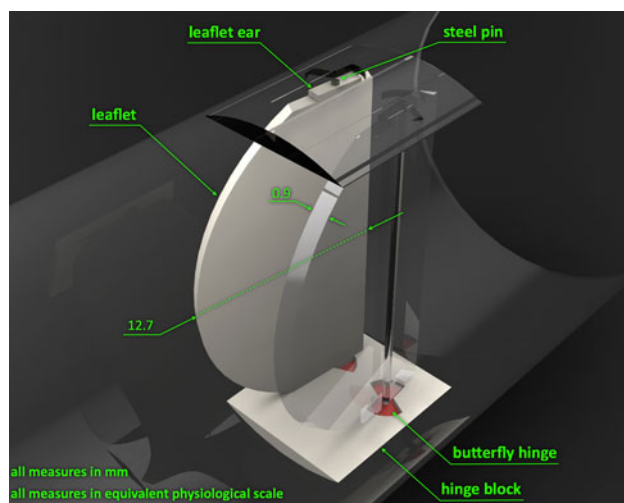

Fig. 3 Schematic diagram of the assembled leaflets and hinge block. Leaflets are in fully open position. Leaflet chord length (12.7 mm) and thickness (0.9 mm) are *highlighted*

design near the circumference of the leaflet. The discs occupy less than 8% of the leaflet area and have a small impact on optical access. The butterfly hinge recesses are cavities in cast epoxy resin hinge blocks. To reduce frictional moment as discussed in Sect. 2, each leaflet includes a pair of steel pins which rotate in holes set inside the butterfly cavities. This design removes sliding contact between the leaflet and hinge surfaces, but is an approximate representation of a real hinge. Although the design embodies correct scaling of leaflet dynamics, the results presented and discussed in this article entail only experiments with unsteady flow through leaflets fixed in fully open position.

Water is used as the blood analogue fluid in the experiment. Although blood is a shear-thinning, non-Newtonian fluid, it behaves as a Newtonian fluid when it flows in tubes with diameter larger than 1 mm and shear rates greater than 100 s^{-1} (Waite and Fine 2007), and Newtonian fluids such as water–glycerol mixtures are widely used to model blood in in vitro studies of MHVs (Kaminsky et al. 2008). In addition, water has a lower viscosity than blood. This is beneficial to the purpose of increasing the temporal resolution, since, according to the preservation of the non-dimensional parameters, it results in a further reduction in frequency (Eq. 4). Furthermore, the viscosity of water does not vary significantly with fluctuations in ambient temperature, as some more viscous and non-Newtonian blood analogue fluids would.

3.2 Design of the test section

The test section is a cylindrical tube as a model for the root of the aorta, the large blood vessel in which the aortic valve is located. The tube wall is 5 mm thick and is made of transparent PMMA to allow optical access. The model valve is located just downstream of the reservoir. This mimics the anatomical arrangement, in which blood flows through the valve from the relatively large left ventricle of the heart. The inlet is flared with a radius equal to 0.3 of the internal diameter, to prevent flow separation as the fluid enters the test section from the reservoir. By placing the valve near the inlet of the tube, the purpose is to produce a relatively uniform upstream velocity profile. This is a better approximation to the in vivo aortic flow conditions than a fully developed velocity profile.

Computational fluid dynamics simulations were carried out to examine the effects of various test-features of the test section on the large-scale flow field and guide the choice of dimensions. Results indicate that in the final design, the upstream and downstream features, including the reservoir, inlet, outlet and outlet hose, have a weak effect on the flow in the test section. In particular, the bend radius of the outlet hose is large enough that asymmetry of the velocity

field in the test section is negligible. The test section design results in a nearly uniform velocity profile upstream of the valve.

The use of a straight tube downstream of the aortic valve in our model omits the geometry of the aortic sinus, but mimics the geometry realised when aortic valve replacement is associated with aortic root reconstruction using a straight conduit graft. The aortic sinus affects the longitudinal pressure gradient in the aorta and thus may affect the flow in the vicinity of the open leaflets. Recent clinical studies have compared the performance of straight conduit grafts and grafts replicating the aortic sinus (Etz et al. 2007; Kirsch et al. 2009; Schoenhoff et al. 2009).

3.3 Flow loop and pump

Upstream of the test section and valve, there is a 160-L polyethylene tank, which is vented to the atmosphere and acts as a reservoir. Downstream, a $\varnothing$50.8-mm hose connects the test section to a computer-controlled piston pump. A transparent viewing box, with 5-mm-thick PMMA walls, surrounds the test section and is filled with water. The purpose of the viewing box is to reduce optical distortion that occurs between the working fluid and the cylindrical test section. The layout of the flow simulator is constrained by the fixed position of the pump and other apparatus in the laboratory. This necessitates a 180° bend in the hose connecting the pump to the test section.

The computer-controlled piston pump was designed and built in-house (Heraty et al. 2008). The piston draws fluid through the test section on the suction stroke and slowly pushes the fluid back through the test section to refill the reservoir on its return stroke. The pump comprises a 1.5-m-long PMMA cylinder with an inner diameter of 140 mm. The tube is secured and sealed between end blocks machined from Delrin[TM] acetal resin. A double-acting nitrile rubber pneumatic seal seals between the piston and the inside of the cylinder. The stainless steel piston rod is driven by a stepper motor through a ball-screw linear actuator. The stepper motor is controlled using National Instruments[TM] MAX and LabVIEW software, via a NI[TM] motion control card.

3.4 PIV apparatus and method

The PIV system used to conduct the experiments described in this work comprises a double-pulse Nd:YAG laser (PIV Gemini model Y100-15, 610127, TSI Inc.), a digital camera with a 1,000 × 1,016 pixel CCD (PIVCAM 10-30, TSI Inc.), an articulated light delivery arm, a synchroniser and a PCI frame grabber. The camera lens (Nikkor) has 70 mm focal length and f/5.6 aperture.

The water flow is seeded with neutrally buoyant hollow silver-coated glass particles of nominal mean diameter 14 μm. Particle apparent density is 1,100 kg/m³, and scanning electron microscopy images show that their size ranges between about 1 and 30 μm. Based on a bulk average velocity of 50 mm/s (model scale) and leaflet thickness of 5 mm (model scale), the Stokes number for these particles is $Stk = 6 \times 10^{-5}$, ensuring accurate flow tracing (reduced Stokes number is a further benefit of scale-up). During the measurements, the seeding particles are illuminated by laser light pulses with wavelength of 532 nm. The duration of each pulse is 6 ns, and each laser has a maximum repetition rate of 15 Hz. A 15-mm concave cylindrical lens and a 500-mm convex spherical lens are used to reshape the laser beam into a light sheet.

Image acquisition and processing are controlled through TSI Insight[TM] 3G software. Pulse separation time is set to 2,060 μs. The particle density in the working fluid is set to give an average of 12 particle images in each 32 × 32 pixel interrogation window. The start of image acquisition is triggered in all experiments by a mechanical sensor on the pump carriage, to ensure repeatable timing. The digitised images are cross-correlated using a recursive rectangular grid algorithm, which uses 32 × 32 pixel and then 16 × 16 pixel interrogation windows to find the mean pixel displacement. A Gaussian peak fit is used to determine the location of the cross-correlation peak to subpixel accuracy. Post-processing comprises a standard deviation filter to remove spurious vectors, followed by an interpolation to fill any empty locations and a Gaussian smoothing.

The mismatch between the refractive indices of water (1.33) and PMMA (1.49) is a source of optical aberration, due to the presence of the cylinder surface, which cannot be everywhere normal to the path of either the incident or the scattered light. To reduce optical distortion, the tube is enclosed in a box of square cross-section filled with water. In addition, in our scaled-up model, the aberration is mitigated by the small ratio of the tube wall thickness (5 mm) to its diameter (140 mm).

All measurements reported in this article were made on the mid-plane of the tube. Image distortion effects were quantified by using the PIV processor with images of a rigid planar object on the measurement plane, taken before and after a known in-plane displacement at an angle of 45° to the tube centreline. Since distortion is due to the presence of the tube, the measurement displacement is investigated as a function of the distance r from the centreline of the tube. Results showed that for $r \leq 55$ mm (79% of tube radius), the measured displacement is independent of r. In this region, any sensitivity to r is insignificant compared to the apparent random fluctuation in the measurement (whose standard deviation is 1.44%). For radial position between 55 and 65 mm (i.e. up to 93% of the tube radius),

the displacement appears no longer uniform, as it increases with r up to a maximum deviation of 6% from the expected displacement. Such deviation becomes even higher for $r > 65$ mm, increasing to 30% of the uniform displacement measured for $r \leq 55$ mm. This test indicates that PIV measurements may be made in the central 79% of the tube without significant errors due to optical distortion.

3.5 Measurement resolution and locations

According to the design choices, the size scaling factor is 5.8 and the viscosity scaling factor is 0.29. Consequently, the velocity in the system is reduced by a factor of 19.1, according to Eq. 3, and the effective measurement sample frequency is increased by a factor of 118. For clarity and in order to ease comparison with data from literature, all values will be reported in equivalent physiological scale, unless stated otherwise.

Measurements were taken for each flow condition in two regions in the x–y mid-plane of the test section, as indicated in Fig. 4. The magnification was set to achieve a field of view of 7.6×7.6 mm. The location labelled as F1 frames the area just downstream of the leaflet tip, while the frame labelled as F2 is shifted by 7 mm in the x direction, so there is small overlap of the two frames. The final interrogation window size is 16×16 pixels, and the corresponding measurement spatial resolution, defined as the distance between velocity vectors, is 120 μm. The temporal resolution is connected to the acquisition rate of the PIV system and benefits from the scaling of geometry and viscosity according to Eq. 4, resulting in a value of 570 μs or an equivalent sample frequency of 1,754 Hz.

Spatial averaging across the light sheet thickness is intrinsic to PIV, and consequently the thickness of the light sheet is a limit on spatial resolution in measurement of three-dimensional flows. The light sheet thickness was measured by illuminating a diffuse surface placed at a 10° angle to t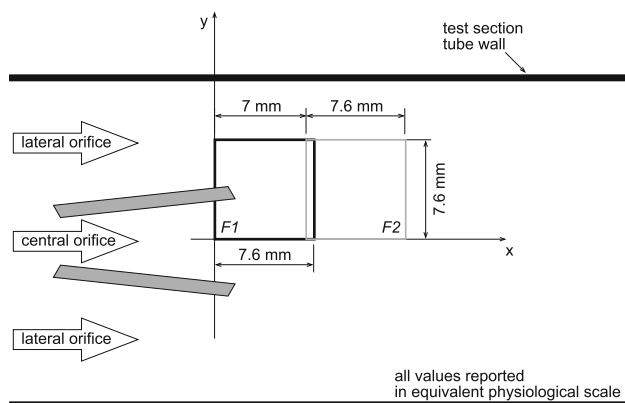he light sheet at the focal point of the spherical lens. An image of the illuminated surface was taken using the PIV CCD camera and analysed to show that over 95% of illumination energy lies in a band of thickness 255 μm. This agrees well with the value of 212 μm specified by the manufacturer and corresponds to 44 μm in equivalent physiological scale. This is much less than the in-plane dimensions of the PIV interrogation regions, equivalent to 120 μm $\times$ 120 μm. Therefore, the measurement volume is thin enough to ensure that averaging over the light sheet thickness does not compromise the actual spatial resolution.

3.6 Error analysis: effect of scaling on PIV measurement accuracy

While the use of a scaled-up experiment is beneficial for measurement resolution (i.e. it raises the spatial and temporal frequency of measurements), its effects on velocity measurement error are not initially obvious. This question is addressed in the analysis summarised here, with full details given in "Appendix".

In most PIV implementations, the reported measured particle velocity is the estimated spatial particle displacement Δx_p divided by the laser pulse separation time τ. A Taylor expansion of the particle position $x_p(t)$ shows that

$$\frac{\mathrm{d}x_p}{\mathrm{d}t} = \frac{\Delta x_p}{\tau} - \frac{\tau}{2}\frac{\mathrm{d}^2 x_p}{\mathrm{d}t^2} + \ldots \qquad (9)$$

where the first term on the right side is the approximate velocity reported by PIV, and the second is the leading term of the temporal discretisation error, which is due to particle acceleration and the effective averaging over the period τ. Error in Δx_p is caused both by spatial discretisation of the measurement plane (which requires averaging over each interrogation window) and by error in the image processing algorithm used to determine displacement. Error in the measurement of τ is considered negligible in comparison with other sources.

The image processing error depends on the chosen algorithm, particle image size, particle seeding density and particle image displacement (e.g. Raffel et al. 1998). The PIV measurement can be configured in both full-scale and scaled-up experiments with optimal choices of these parameters (which can be controlled independently of the flow under measurement). Thus, scale-up does not affect the error in particle image displacement (in pixels) due to image processing.

The two remaining sources of error are the spatial and temporal discretisation effects. They are analysed in detail in Appendix by Taylor series expansions for scale-up of a flow field according to the rules developed in Sect. 2 earlier. It is demonstrated that the spatial and temporal discretisation errors are reduced by factors of $(D'/D)^2$ and

Fig. 4 The experimental measurement locations, labelled *F1* and *F2*

D'/D, respectively, or 33.6 and 5.8 for the experiments presented in this paper.

3.7 Test conditions

Measurements have been conducted under two test conditions. In the impulsively started condition, the flow is rapidly accelerated from quiescent state to a Reynolds number (based on diameter) of $Re_D = 6,000$. The total duration of the measurement is 19.3 s (model scale), equivalent to 164 ms in physiological scale and corresponding to 290 image pairs collected. Steady state flow rate is reached in about 3% of the total duration by a period of uniform acceleration. In the other unsteady flow condition, referred to as the systolic condition, the piston motion follows a physiologically realistic aortic velocity waveform based on that used by Brucker et al. (2002), scaled to a peak Reynolds number of 6,000. Each measurement consists of a 650-frame time sequence in the systolic (forward arterial flow) phase, whose duration is 370 ms. Peak flow rate occurs 90 ms after the start time. For both steady and systolic flow, the leaflets are fixed in the open position for the duration of the experiment.

4 Results

4.1 Instantaneous velocity and vorticity fields

Velocity vectors and instantaneous vorticity contours are reported in Figs. 5 and 6. Vorticity contours are plotted in blue (clockwise rotation) and red (counterclockwise rotation). In the following the terms, *central orifice* and *lateral orifice* (Yoganathan et al. 1992) are used as illustrated in Fig. 4.

Figure 5 highlights fluid behaviour during the early part of the impulsively started flow and the acceleration stage of the systolic flow. In the former case, flow is initially attached on both sides of the leaflet and vortex shedding is observed in the wake. By $t = 32$ ms, the flow has undergone separation on the suction (downstream-facing) surface of the leaflet. At $t = 58$ ms, a large vortex detaches from the suction surface and initiates alternate vortex shedding. In the case of the systolic flow, the milder acceleration produces a different evolution. The wake initially exhibits a steady recirculation zone, which gradually grows as the flow accelerates. Flow separation occurs at about $t = 60$ ms and is soon followed by alternate vortex shedding, as in the case of the impulsively started flow.

The further evolution of the systolic flow is illustrated in Fig. 6. From $t = 65$ ms to $t = 105$ ms, periodic vortex shedding takes place. After this time, we observe disorganised structures whose vorticity gradually decreases as the flow decelerates. Trailing-edge vortices are shed until about $t = 250$ ms.

4.2 Temporal evolution of flow velocity

Histories of the *x*-component of velocity in the impulsively started flow are reported in Fig. 7 for a number of selected locations. The dashed line represents the instantaneous mean velocity, equal to the pumping piston velocity. In the
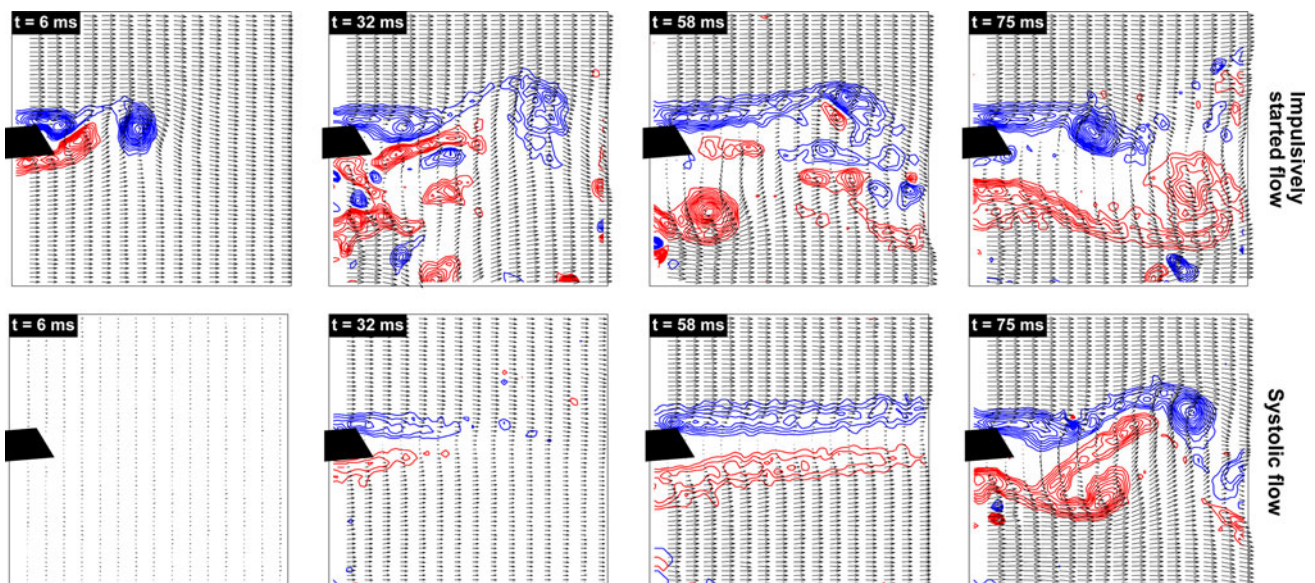

Fig. 5 Velocity vectors and vorticity contours in the early stages of the impulsively started flow (*top row*) and the systolic flow (*bottom row*). *Blue* and *red* colours are used for positive and negative vorticity, respectively. For clarity, only contours of absolute vorticity above 500 s^{-1} are plotted. A sketch of the leaflet tip is superimposed
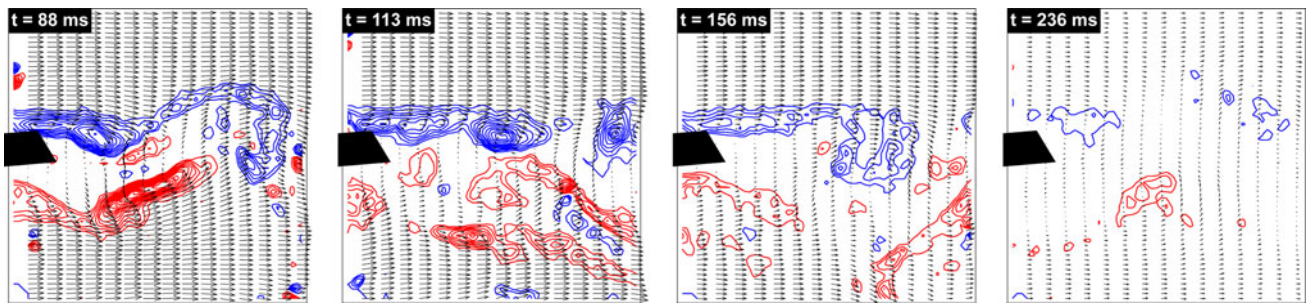
Fig. 6 Velocity vectors and vorticity contours near peak flow ($t = 90$ ms) and in deceleration of systolic flow. *Blue* and *red* colours are used for positive and negative vorticity, respectively. A sketch of the leaflet tip is superimposed
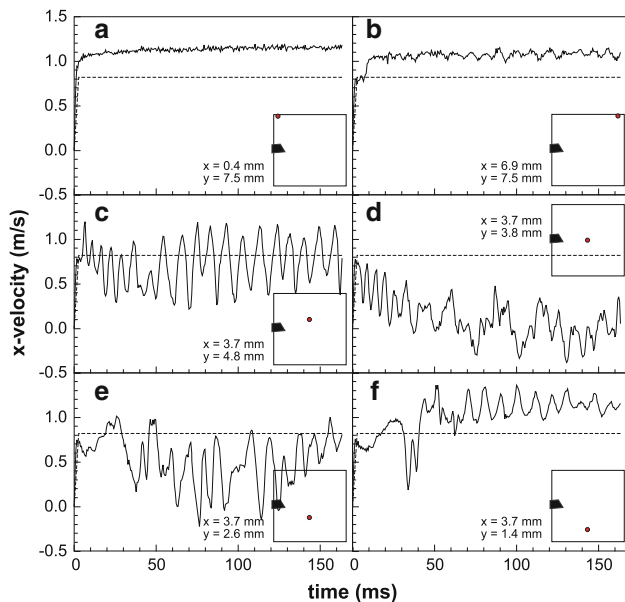

Fig. 7 Time history of the *x*-component of velocity for the impulsively started flow. The *dashed line* is the imposed velocity profile

Fig. 8 Time history of the *x*-component of velocity for the unsteady systolic flow. The *dashed line* is the imposed aortic waveform

lateral orifice jet (locations *a* and *b*), the velocity quickly reaches a steady state value which is higher than the imposed mean velocity, since the leaflet forms a converging channel. Later, and downstream of the valve (location *b*), the velocity shows larger fluctuations. At location *c*, the velocity undergoes large fluctuations between 0.3 and 1.2 m/s. From $t = 50$ ms to the end of the measurement, the oscillations appear periodic. Locations *d* and *e* are close to location *c*, but the velocity profiles are different insofar as the values are lower (including negative values) and the fluctuations are not periodic. At location *f*, in the central orifice jet, the velocity profile shows a complex behaviour up to about $t = 50$ ms, similar to location *e*, and later resembles the behaviour of locations *a* and *b*, but with more severe oscillations.

Figure 8 reports the temporal profiles of the *x*-component of velocity for the systolic flow. For the locations in the lateral orifice jet (*a* and *b*), the velocity profile closely
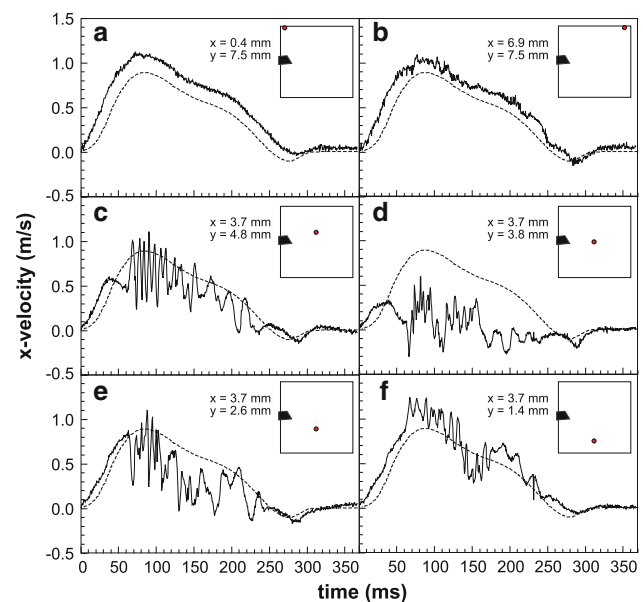
resembles the imposed aortic waveform, although at location *b* we observe fluctuations. For locations *c* and *d*, directly downstream of the leaflet tip, the velocity drops suddenly at $t = 40$ ms (middle acceleration), becoming negative at the latter location. Strong periodic oscillations are observed at location *c* for about 40 ms about the systolic peak. Later in the deceleration phase, the fluctuations appear less regular. In the central orifice jet (location *f*), the flow follows the prescribed waveform more closely, but shows stronger fluctuations than in the lateral orifice jet.

Spectral analysis is used to provide quantitative support to the observed temporal evolution of the flow. Yarusevych et al. (2006) found that spectra of the transverse velocity component were more sensitive than the spectra of the streamwise component in flow over an aerofoil; spectra of transverse velocity are therefore preferred for the following analysis. Results suggest a general trend that is common to most of the spatial locations in the area investigated. In

terms of dominant frequencies, the spectra are similar over a large area surrounding the leaflet wake, with the notable exception of the locations on the upstream (left) side of the field of view, where no dominant peak is detected. For conciseness, therefore, the spectra $\bar{E}_{vv}$ presented are averaged over the entire space domain and calculated over the entire time sequence (290 time points for the impulsively started flow and 650 time points for the systolic flow). The spectra for the two flow cases, reported in Fig. 9, exhibit a number of peaks, followed by a range of power-law decay with exponent close to $-5/3$. The two spectra tend to become flat at high frequency, as an effect of measurement noise on the velocity data (Ganapathisubramani et al. 2007).

In the impulsively started flow (Fig. 9a), the spectrum shows a peak centred at $f = 110 (\pm 6)$ Hz (where the uncertainty ± 6 Hz depends on the sample frequency and record length). The corresponding Strouhal number is $St_d = f \cdot d/U = 0.17$, where d is the projection of the leaflet length on the cross-stream plane and U is the maximum freestream velocity (Huang et al. 2001). In addition to the results shown, the spectrum has been evaluated for two distinct time subsets, namely acceleration and the constant flow rate. Results show that the peak at 110 Hz is absent during the acceleration stage, showing that this is the frequency of the vortex shedding established in the wake as the freestream velocity becomes steady. A distinct peak at $f = 171 (\pm 6)$ Hz ($St = 0.26$), visible in Fig. 9a, appears only in acceleration and is related to the oscillations clearly visible at the beginning of the signal reported in Fig. 7d and the vortex shedding observed prior to flow separation (Fig. 5, $t = 6$ ms). These oscillations last longer than the acceleration stage, and flow separation eventually occurs when the freestream velocity has already become steady.

The spectrum $\bar{E}_{vv}$ for the systolic flow exhibits more peaks. The three peaks highlighted in Fig. 9b are centred at $f = 51, 114$ and $152 (\pm 3)$ Hz, and spectra for time subsets (not shown) confirm that each is related to a distinct stage

of the flow. Here, the uncertainty is smaller because of the larger record length. The first period considered, up to $t = 60$ ms, covers early acceleration and shows no significant peaks. The second subset, up to $t = 120$ ms, includes the highest freestream velocities and exhibits a peak at 152 Hz ($St = 0.23$), which is therefore the frequency of the vortex shedding shown in Figs. 5 and 6 ($t = 75$ ms and $t = 88$ ms). Notably, this frequency is higher than the frequency detected for the impulsively started flow at the same Reynolds number. The third time subset is taken from $t = 120$ ms to $t = 170$ ms and covers the middle deceleration stage. Here, the main peak is centred at 114 Hz, which is quite close to the value found for the impulsively started flow. Finally, in the late deceleration stage ($t > 120$ ms), there is a peak centred at 51 Hz.

4.3 Instantaneous shear stress fields

The instantaneous shear stresses are of interest for their role in blood damage. They are evaluated from PIV results for the systolic flow only, according to the relation

$$\tau = \mu \left(\frac{\partial u}{\partial y} + \frac{\partial v}{\partial x} \right) \qquad (10)$$

where u and v are, respectively, the x and y components of the flow velocity. The gradients are approximated by a central difference operator. The shear stresses are reported in Fig. 10 for a number of time steps. Contours between 1 and 8 Pa only are plotted to make the figures more readable. Locations F1 and F2 are plotted together, but the two measurements were collected separately and hence are not correlated.

During the acceleration stage, the leaflet boundary layers separate from the trailing edge to form free shear layers on both sides of the leaflet tip, with high-shear stresses. Larger stresses are measured on the pressure (upper) surface of the leaflet. At this stage ($t = 58$ ms), shear stress is not larger than 0.5 Pa anywhere but in the narrow band between $y = 2$ mm and $y = 5$ mm. After the inception of

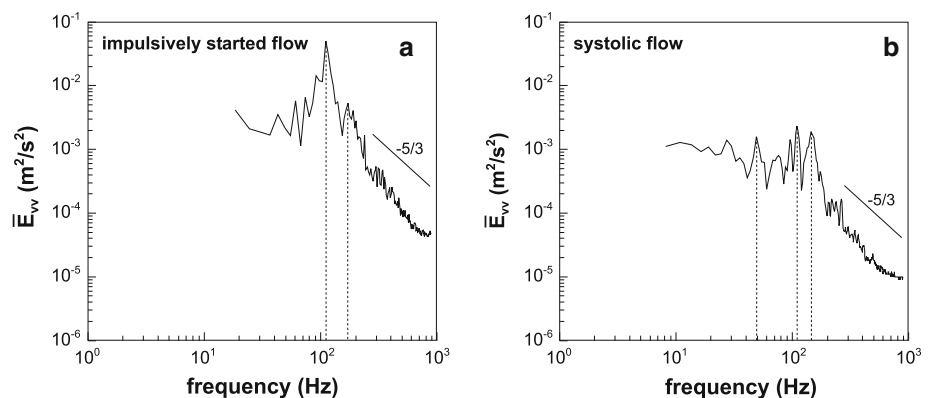**Fig. 9** Space-averaged spectra of the transverse velocity component for both flow conditions

Fig. 10 Shear stress contour plots at six selected times in frames *F1* and *F2* as defined in Fig. 3. A sketch of the leaflet tip is superimposed
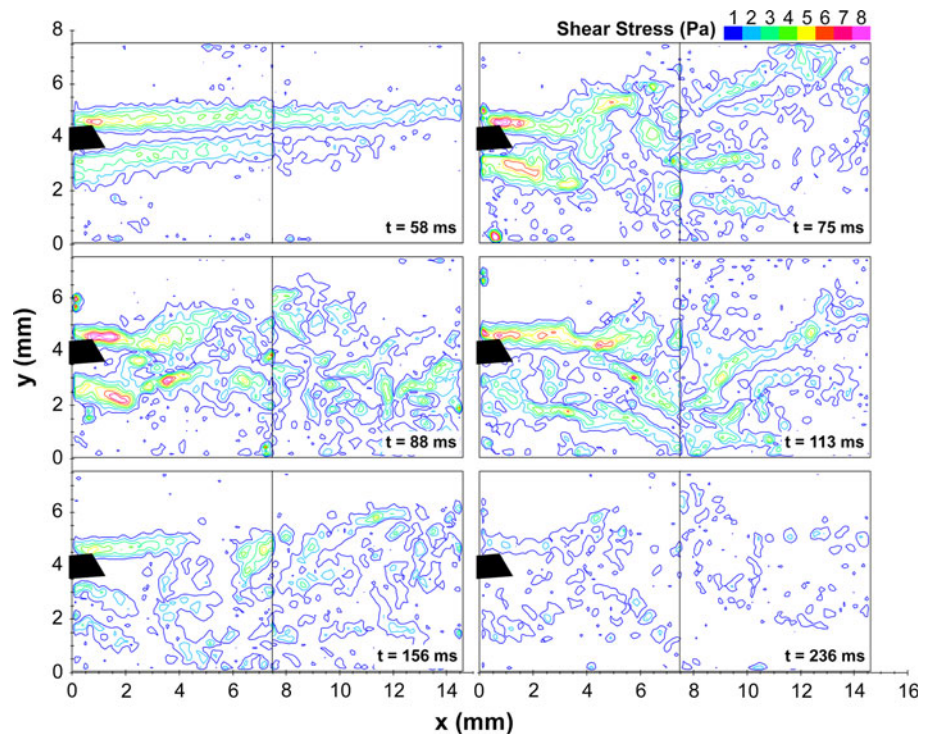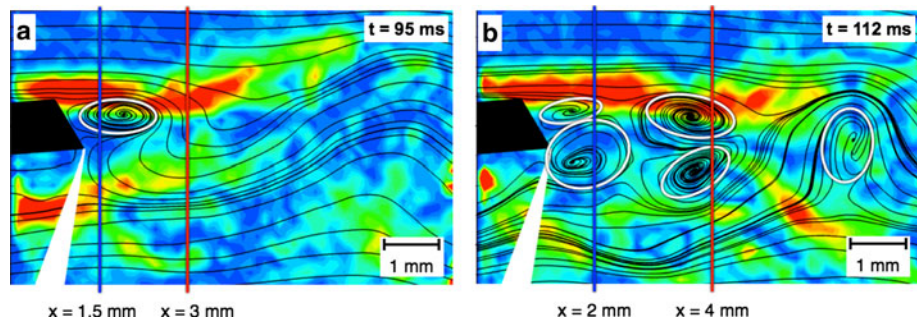

Fig. 11 Close-up of the instantaneous shear stress contour plot at **a** *t* = 95 ms and **b** *t* = 112 ms. The *ellipses* in *white* enclose the vortices generated in the wake

vortex shedding, the appearance of the high-shear area changes from elongated continuous threads to unevenly distributed, fragmented clumps ($t = 75$ ms and $t = 88$ ms). These high-shear structures are shed from both surface and trailing-edge vortices and exceed 7 Pa near the leaflet. During flow deceleration ($t = 113$ ms onwards), shear stress becomes highly non-uniform in the central orifice, reflecting the vorticity distribution presented in Sect. 4.2. At $t = 156$ ms, the shear stress reaches 5 Pa in the wake, and at $t = 236$ ms, it is never larger than 4 Pa.

Figure 11 shows a close-up view of the instantaneous shear stress field near the leaflet tip just after peak flow ($t = 90$ ms), with instantaneous streamlines superimposed. The length scale of visible vortices (highlighted by ellipses) ranges from 400 to 1,000 μm. Profiles of shear stress are plotted in Fig. 12 on constant x lines marked in Fig. 11. The distances between the most prominent minima and maxima of stress (corresponding to the vortices visible in

Fig. 11) are 500–700 μm, consistent with the length scales observed for the vortices themselves.

5 Discussion

A scaled-up model mechanical heart valve has been designed and built, and used to conduct PIV measurements of the velocity field at a spatial resolution equivalent to 120 μm (distance between velocity vector measurements) and measurement frequency equivalent to 1,750 Hz. The scale-up approach has been established theoretically by dimensional analysis, and it has been shown that the various types of measurement error in PIV are reduced or unaffected by scale-up. Implementation of the concept entails unconventional techniques for PIV, including the use of water in place of a more viscous blood analogue fluid to further enhance temporal resolution, and a thin-walled model to
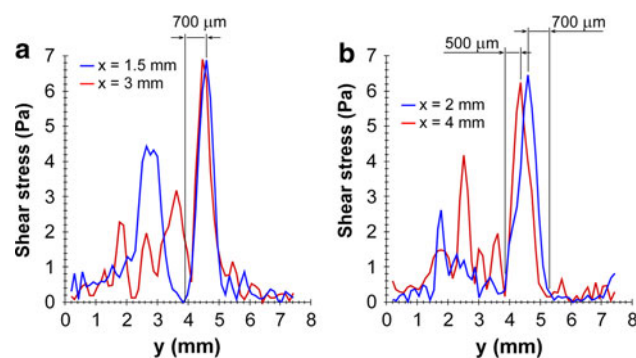
Fig. 12 Shear stress profiles along the *vertical lines* illustrated in Fig. 10

minimise optical aberration without matching the refractive index of fluid and walls.

In the present work, this technique has been applied only to measurement planes on the tube mid-plane. For possible extension to off-centre measurements, effects of refraction must be considered for both illumination and imaging. Simple ray-tracing calculations show that the light sheet may be positioned up to $z/R \cong 0.76$ (where R is the tube radius and z is the coordinate normal to the light sheet). Beyond this, illumination is not possible because of total internal reflection. At this extreme configuration, the light sheet inside the tube will deviate by approximately 7° from the incident direction, but this can easily be corrected by steering of the incident light. The light sheet thickness may also be affected by refraction through the tube wall, since rays within the light sheet will experience non-uniform refraction. At $z/R \cong 0.76$, a parallel light sheet of thickness 250 μm would diverge up to a thickness of around 520 μm, as it crosses the tube. At $z/R = 0.71$, the maximum resulting thickness would be less than 350 μm, which is acceptable for most applications. A light sheet may be delivered through transparent moving leaflets, if the illumination direction is accurately aligned normal to the leaflets' axis of rotation.

In experiments on the effects of image distortion, it has been shown that PIV errors for mid-plane measurements are unaffected by optical aberrations over the central 79% of the tube. Imaging performance is expected to be better for measurement planes closer to the camera, since the light scattered from any particle will encounter smaller values and range of angle of incidence at the tube wall. Imaging will not be affected by leaflet motion, as long as the viewing direction is parallel to the leaflets' axis of rotation. Thus, the present technique is not restricted to measurements on the mid-plane or to fixed leaflets, by either the illumination or imaging systems. Although a light sheet cannot be positioned near the inner surface of the tube (e.g. to measure flow near the hinges on a plane normal to the leaflet rotation axis), PIV can be conducted

over most of the tube diameter with the methods described here. It is only the relatively small thickness of the tube wall that makes PIV possible under these conditions of strong refractive index mismatch.

The technique has been applied to investigate the development of the unsteady flow-field downstream of an open bileaflet mechanical heart valve (MHV). The spatial resolution of the measurements presented in this paper is 120 μm, achieved without interrogation region overlap. The finest vector spacing reported previously is 135 μm (Dasi et al. 2007; Ge et al. 2008) with 50% overlap of interrogation regions (i.e. interrogation region of 270 μm) and measurement frequency of 1.2 Hz (50 Hz time sequences were reconstructed from a sequence of independent measurements). In a resolution-sensitivity study based on the methodology of computational mesh-sensitivity studies, Ge et al. (2008) studied the variation of computed shear stress while reducing the distance (or increasing the overlap) between PIV interrogation regions (velocity sample points). They found only small variation between results on the finest (50% overlap) and second finest (zero overlap) samplings. This result suggests indirectly that the interrogation window size of 270 μm is fine enough to resolve all structure in the flow. However, it can be shown by a Taylor series analysis (assuming, as Ge et al. did, that each PIV velocity sample represents a uniform average over the interrogation region) that this estimate of shear stress does not converge as the distance between interrogation window centres is reduced, because the interrogation window size is held constant. Thus, this evidence for identification for the smallest scales is not rigorous. As discussed in the Introduction, knowledge of the small-scale flow structure is necessary if the links between fluid dynamics and cell-mediated disease are to be understood. Structures of less than 400 μm in diameter have been observed in the present work.

Since the valve leaflets are fixed in the present model, flow phenomena due to valve opening and closure are not reproduced. Observation of leaflet kinematics indicates that valve opening and closure actually occur in a very short time (Dasi et al. 2007), so leaflets are fully open during most of systole. The specific subject of the current investigation is the small-scale flow structures that are caused by the leaflet wake and interact directly with cells, and these are unlikely to be affected by the opening of the leaflet, which is already complete shortly after the beginning of systole.

Scale-up yields enhancements in temporal as well as spatial resolution. The current effective measurement frequency is 1,750 Hz. The highest reported to date for PIV on an MHV is 3,000 Hz (Kaminsky et al. 2008), recorded at a spatial resolution one order of magnitude coarser than the experiments presented here. The scale-up

approach enables extremely high resolution with basic PIV apparatus.

Shear stress is an important parameter in the performance of cardiovascular devices including MHVs, as it modulates biomechanical blood cell responses including thrombosis and haemolysis. Measurements of the viscous stress in systolic flow have been presented. The results show that during acceleration, the highest shear stresses are concentrated in a 3-mm-thick band containing steady shear layers in the leaflet wake. The stress peaks up to over 7 Pa, consistent with the value of 10 Pa reported by Ge et al. (2008) in experiments conducted using PIV in a physiological-scale bileaflet valve in similar flow conditions and comparable spatial resolution. After flow separation, high stress is concentrated in structures shed from the wake of the leaflet.

In geometric terms, the leaflet of an MHV is a semi-elliptical flat plate at a low angle of attack, with a thickness-to-chord ratio of 6.5% and chord Reynolds number $Re_C = 3{,}240$ at peak flow in the conditions tested here. Flow remains attached on both sides of the leaflet for most of the acceleration stage. When separation eventually occurs, the growth and detachment of a vortex on the downstream-facing or suction surface of the leaflet initiate an alternate shedding of trailing edge and surface vortices in the wake. These qualitative observations reveal a strong analogy with flow over an impulsively started wing at Reynolds numbers below 3,000 (Huang et al. 2001).

It has been proposed that the free shear layers and vortices in the leaflet wakes are responsible for the onset of transitional or turbulent flow downstream of the valve (Dasi et al. 2009) and the formation of free emboli (potentially harmful particles of clotted blood) in the aorta (Bluestein et al. 2000). Investigation into leaflet vortex shedding has been enhanced here by the high effective temporal resolution of the measurements.

The experiments presented in the paper demonstrate the appearance of flow separation on the inner surface of the valve leaflet, resulting in the onset of vortex shedding. The phenomenon is highlighted in Fig. 13, which shows the velocity field near the leaflet. Here, reverse velocity in the boundary layer is clearly visible. Flow separation determines the occurrence of vortex shedding and is closely related to the pressure field, which is in turn influenced by the geometry of the aortic root. In our experiments, we mounted the valve in a straight duct, reproducing a geometry that is not unusual, since partial or total reconstruction of the aortic root is often associated with valve replacement. Nonetheless, to clarify the effect of the simplified duct geometry on leaflet flow separation, we consider the results of numerical simulations presented by Bluestein et al. (2000) for a duct with aortic sinuses. In those computations, the flow is unsteady and the input
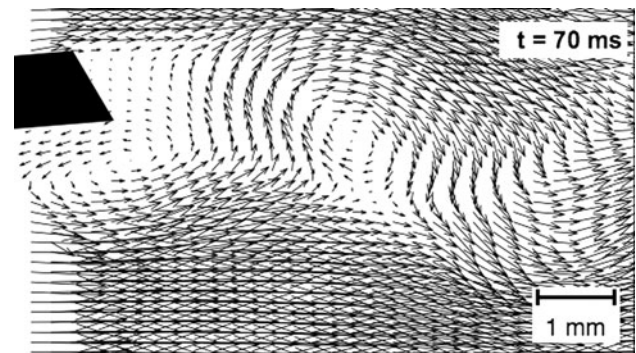

Fig. 13 Detail of the flow field near the valve leaflet during flow acceleration ($t = 70$ ms)

velocity waveform is very close to that in our experiments. Comparison of the flow field calculated by Bluestein et al. and the results reported here in Fig. 13 show that flow separation of the leaflet boundary layer occurs either when aortic sinuses are modelled or when a straight tube is used. To the authors' knowledge, the experimental results presented here are the first that provide a detailed visualisation of flow separation in the leaflet's boundary layer, thanks to the high spatial resolution and excellent optical access provided by the present approach.

Results for realistic systolic flow were compared with behaviour of an impulsively started flow to examine the effect of unsteady bulk flow on the wake. At the beginning of acceleration, the flow is attached for both cases. In the impulsively started flow, a vortex is shed immediately at the beginning and separation occurs before $t = 32$ ms. In the systolic flow, with milder acceleration, the wake remains narrow and almost parallel until flow separation occurs at about $t = 60$ ms. After flow separation, alternating vortex shedding is initiated at a frequency of 152 Hz (corresponding to $St_d = 0.23$). This frequency is detected about the peak of the systolic waveform and is significantly higher than in the case of the impulsively started flow at the same Reynolds number (110 Hz, $St_d = 0.17$). The latter value is close to the range 0.12–0.16 reported in literature for impulsively started flow over an inclined flat plate with $Re_C < 500$ (Taira and Colonius 2009). The discrepancy in vortex shedding frequency may be due to the fact that in the systolic flow, separation occurs when the freestream velocity is still increasing, so it can benefit from the stabilizing effect of acceleration (Schlichting 1979) resulting in a smaller reverse flow region. This, in turn, results in smaller vortices and therefore higher shedding frequency.

By the Nyquist criterion, a flow feature must be at least twice as large as the vector spacing to be resolved by PIV; therefore, the minimum size detectable in the present experiments is about 240 μm. Length scales as small as 400 μm, approaching this resolution limit, were clearly detected in the results. The existence of smaller scales has

been suggested based on calculation of the Kolmogorov scale (Liu et al. 2000). However, it has not been established whether the assumptions underlying Kolmogorov's theory are valid in this short-duration flow of relatively low Reynolds number, and the smallest flow structures have yet to be directly observed. An extension of the current technique to higher resolution, by the use of higher optical magnification, will assist in this effort.

The results indicate that the flow downstream of the leaflet, even at peak systolic flow, is not capable of triggering red blood cell damage, which occurs above shear stresses of the order of hundreds of Pa (Leverett et al. 1972; Sutera and Joist 1992). On the other hand, the measured shear stresses are quite close to the lower limit for platelet activation leading to thrombosis (Kroll et al. 1996).

6 Conclusions

A novel scaled-up mechanical heart valve has been designed and used to measure the flow-field downstream of the leaflet tip with particle image velocimetry. Geometric scale-up and choice of test liquid enabled increase in effective spatial and temporal resolution by factors of 5.8 and 118, respectively. While the principle of scaling up a biomedical flow device is not novel, in this paper it has been developed with a rigorous theoretical analysis of the proper scale-up, accounting for rigid-body dynamics and friction, and of the effect of scaling on measurement error. On this basis, we have been able to improve the resolution of PIV measurements beyond the current limits for mechanical heart valves. In addition to the substantial resolution improvements, the scale-up is also beneficial for PIV accuracy, since the spatial and temporal discretisation errors are respectively 33.6 and 5.8 times smaller than in optimised physiological-scale experiments.

The shear stresses measured using PIV results are consistent with recent results in the literature at similar conditions and indicate that the systolic flow conditions are close to the lower limit for initiating thrombosis. The temporal resolution of the new measurements is sufficient to investigate the evolution of leaflet wake flow regimes and quantify vortex shedding. Spectral analysis has demonstrated that shedding frequency is similar to that observed for inclined flat plates in comparable flow conditions (low Reynolds number, impulsively started flow). Notably, the flow exhibits a different behaviour in systolic conditions, where the milder acceleration results in significantly higher shedding frequency. This result highlights the sensitivity of valve hemodynamic performance to the velocity waveform, confirming the need for realistic unsteady flow conditions.

The spatial resolution of 120 μm sets the minimum detectable wavelength of 240 μm. Preliminary analysis revealed active length scales down to that resolution limit. This result cannot exclude the possibility of smaller structures, whose investigation requires a further increase in resolution. In this paper, we have demonstrated the potential of the scale-up method to support enhanced resolution. This establishes the proposed approach for future measurement at even higher resolution (through higher optical magnification and tracer particle density), in order to shed light on the smallest flow structures in prosthetic device flow.

Appendix

Effect of scale-up on spatial and temporal discretisation error

As outlined in Sect. 3.6, scale-up may impact on PIV measurement error due to spatial and temporal discretisation. Here, we compare the magnitude of each category of error for the full-scale and scaled-up flows.

It is assumed that both the full-scale and scaled-up experiments are optimised for maximum resolution and accuracy with the same equipment; thus, the interrogation window size (in pixels) and optical magnification M are equal in both cases. Particle image size is manipulated to the same optimal value in both cases, by choice of particles and/or defocusing. The optimal laser pulse separation time τ, however, is not the same for both experiments. It should be chosen such that the particle image displacement is the same in both experiments, even though particle velocity is scaled according to Eq. 3. Therefore, the scaling of the pulse separation time is

$$\tau' = \frac{MU}{MU'}\tau = \frac{\mu D'}{\mu' D}\tau. \tag{11}$$

The scaling of τ is different from the scaling of the physical time t given by Eq. 4.

Spatial discretisation error

This error arises because the velocity at a location x (we consider a one-dimensional space for clarity) is actually calculated as a weighted average over a finite interrogation window of width h. The computed particle displacement in the image plane, $\Delta s_p = M\Delta x_p$, is given by

$$\Delta s_p = \int_{-h/2}^{h/2} q(s)W(s)\mathrm{d}s \tag{12}$$

where s is the coordinate in image space, $q(s)$ is the true particle image displacement field, and $W(s)$ is an unknown weighting function which accounts for the diverse contribution from different parts of the interrogation window (for example, the signal is high near bright particles, zero where there are no particles, and low near the edge of the interrogation region, where a particle may not appear in both images). In PIV, we approximate the pointwise displacement $q_0 = q|_{s=0}$ at the centre of the interrogation window with the average Δs_p calculated over the interrogation window. The error can be estimated by expanding $q(s)$ in Eq. 12 as a Taylor series in s, noting that the weight function has integral equal to 1 and is symmetric, so that odd moments vanish. The result gives the relative error, truncated at the first term, as

$$\frac{\varepsilon_{\Delta s}}{\Delta s_p} = \frac{|\Delta s_p - q_0|}{\Delta s_p} \cong \frac{1}{2\Delta s_p} \frac{\mathrm{d}^2 q}{\mathrm{d}s^2}\bigg|_{s=0} \int_{-h/2}^{h/2} s^2 W(s)\mathrm{d}s. \tag{13}$$

Now, we consider the effect of scale-up on this error. Since the PIV configuration is similarly optimised in both full-scale and scaled-up experiments as discussed in Sect. 3.6, the particle image displacements are independent of scaling (i.e. $\Delta s'_P = \Delta s_p$) as is the integral on the right-hand side of Eq. 13.

In principle, with sufficiently high scale-up, the flow velocity would become uniform within the interrogation window, and the spatial derivatives of the displacement field $q(s)$ would vanish. Scaling up the experiment means stretching the spatial scale of the velocity gradients. Noting that $q = MU\tau$ and $\frac{\mathrm{d}(\bullet)}{\mathrm{d}s} = \frac{1}{M}\frac{\mathrm{d}(\bullet)}{\mathrm{d}x}$, the second derivative in Eq. 13 can be written in terms of object space variables (U and x), and compared for full-scale and scaled-up experiments to show that

$$\frac{\mathrm{d}^2 q'}{\mathrm{d}s'^2} = \left(\frac{D}{D'}\right)^2 \frac{\mathrm{d}^2 q}{\mathrm{d}s^2} \tag{14}$$

and therefore, the relative error due to spatial discretisation scales as

$$\frac{\varepsilon'_{\Delta s}}{\Delta s'} = \left(\frac{D}{D'}\right)^2 \frac{\varepsilon_{\Delta s}}{\Delta s}. \tag{15}$$

Thus, the spatial averaging error is favourably affected by scaling: the error is $(D'/D)^2$ smaller in the scaled-up experiments. If the weighting function $W(s)$ is not symmetric, contrary to the assumption earlier, then the factor reduces to D'/D.

Temporal discretisation error

The relative error due to temporal discretisation can be expressed, according to Eq. 9, as

$$\frac{\varepsilon_U}{U} = \frac{\tau}{2U} \frac{\mathrm{d}^2 x_p}{\mathrm{d}t^2}. \tag{16}$$

The particle acceleration term incorporates both local and convective acceleration and may become significant either in strongly unsteady flows where the timescale of velocity fluctuations is comparable with τ or if the length scale of spatial structure is comparable with h. Since pulse separation time τ must be increased to allow for lower velocity in the scaled-up model (Eq. 11), it is necessary to investigate this error more closely.

Following Eq. 16, the error in the scaled-up setting is

$$\frac{\varepsilon'_U}{U'} = \frac{\tau'}{2U'} \frac{\mathrm{d}^2 x'_p}{\mathrm{d}t'^2}. \tag{17}$$

Using the scaling laws, $x'_p(t') = (D'/D)x_p(t)$ and $t' = (D'/D)^2(\mu/\mu')t$ as well as Eqs. 3 and 11, the error in full-scale and scaled-up experiments can be compared with the result that

$$\frac{\varepsilon'_U}{U'} = \frac{D}{D'} \frac{\varepsilon_U}{U}. \tag{18}$$

Thus, the temporal discretisation error is influenced by scaling and is reduced by a factor of D'/D in the scaled-up experiment, despite the required increase in pulse separation time.

References

Affeld K, Walker P, Schichl K (1989) The use of image processing in the investigation of artificial heart valve flow. ASAIO Trans 35:294–298

Alam M, Zhou Y, Yang H, Guo H, Mi J (2010) The ultra-low Reynolds number airfoil wake. Exp Fluids 48:81–103

Balducci A, Grigioni M, Querzoli G, Romano G, Daniele C, D'Avenio G, Barbaro V (2004) Investigation of the flow field downstream of an artificial heart valve by means of PIV and PTV. Exp Fluids 36:204–213

Baldwin JT, Deutsch S, Geselowitz DB, Tarbell JM (1994) LDA measurements of mean velocity and Reynolds stress fields within an artificial heart ventricle. J Biomech Eng 116:190–200

Bluestein D, Rambod E, Gharib M (2000) Vortex shedding as a mechanism for free emboli formation in mechanical heart valves. J Biomech Eng 122:125–134

Brucker C, Steinseifer U, Schroder W, Reul H (2002) Unsteady flow through a new mechanical heart valve prosthesis analysed by digital particle image velocimetry. Meas Sci Technol 13:1043–1049

Chahine GL (1996) Scaling of mechanical heart valves for cavitation inception: observation and acoustic detection. J Heart Valve Dis 5:207–214

Dasi L, Ge L, Simon H, Sotiropoulos F, Yoganathan AP (2007) Vorticity dynamics of a bileaflet mechanical heart valve in an axisymmetric aorta. Phys Fluids 19:1–17

Dasi L, Simon H, Sucosky P, Yoganathan AP (2009) Fluid mechanics of artificial heart valves. Clin Exp Pharmacol 36:225–237

Dooley P, Quinlan N (2009) Effect of eddy length scale on mechanical loading of blood cells in turbulent flow. Ann Biomed Eng 37:2449–2458

Ellis JT, Wick T, Yoganathan AP (1998) Prosthesis-induced hemolysis: mechanisms and quantification of shear stress. J Heart Valve Dis 7:376–386

Etz CD, Homann TM, Rane N, Bodian CA, Di Luozzo G, Plestis KA, Spielvogel D, Griepp RB (2007) Aortic root reconstruction with a bioprosthetic valved conduit: a consecutive series of 275 procedures. J Thorac Cardiovasc Surg 133:1455–1463

Figliola RS, Mueller TJ (1981) On the hemolytic and thrombogenic potential of occluder prosthetic heart valves from in vitro measurements. J Biomech Eng 103:83–90

Fung YC (1993) Biomechanics: mechanical properties of living tissues, 2nd edn. Springer, New York

Ganapathisubramani B, Lakshminarasimhan K, Clemens N (2007) Determination of complete velocity gradient tensor by using cinematographic stereoscopic PIV in a turbulent jet. Exp Fluids 42:923–939

Gao Z, Hosein N, Dai F, Hwang N (1999) Pressure and flow fields in the hinge region of bileaflet mechanical heart valves. J Heart Valve Dis 8:197–205

Ge L, Dasi L, Sotiropoulos F, Yoganathan AP (2008) Characterization of hemodynamic forces induced by mechanical heart valves: Reynolds vs. viscous stresses. Ann Biomed Eng 36:276–297

Gott VL, Alejo DE, Cameron DE (2003) Mechanical heart valves: 50 years of evolution. Ann Thorac Surg 76:2230–2239

Healy TM, Fontaine AA, Ellis JT, Walton SP, Yoganathan AP (1998) Visualization of the hinge flow in a 5:1 scaled model of the medtronic parallel bileaflet heart valve prosthesis. Exp Fluids 25:512–518

Heraty K, Laffey J, Quinlan N (2008) Fluid dynamics of gas exchange in high-frequency oscillatory ventilation: in vitro investigations in idealized and anatomically realistic airway bifurcation models. Ann Biomed Eng 36:1856–1869

Huang RF, Wu P, Jeng JH, Chen RC (2001) Surface flow and vortex shedding of an impulsively started wing. J Fluid Mech 441:265–292

Kameneva MV, Burgreen GW, Kono K, Repko B, Antaki JF, Umezu M (2004) Effects of turbulent stresses upon mechanical hemolysis: experimental and computational analysis. ASAIO J 50:418–423

Kaminsky R, Kallweit S, Weber H, Claessens T, Jozwik K, Verdonck P (2007) Flow visualization through two types of aortic prosthetic heart valves using stereoscopic high-speed particle image velocimetry. Artif Organs 31:869–879

Kaminsky R, Kallweit S, Rossi M, Morbiducci U, Scalise L, Verdonck P, Tomasini E (2008) PIV measurements of flows in artificial heart valves. In: Schroder A (ed) Particle image velocimetry: new developments and recent applications. Springer, Berlin, pp 55–72

Kelly SG, Verdonck PR, Vierendeels JA, Riemslagh K, Dick E, Van Nooten GG (1999) A three-dimensional analysis of flow in the pivot regions of an ATS bileaflet valve. Int J Artif Organs 22:754–763

Kidane AG, Burriesci G, Cornejo P, Dooley A, Sarkar S, Bonhoeffer P, Edirisinghe M, Seifalian AM (2009) Current developments and future prospects for heart valve replacement therapy. J Biomed Mater Res B Appl Biomater 88:290–303

Kirsch MEW, Ooka T, Zannis K, Deux JF, Loisance DY (2009) Bioprosthetic replacement of the ascending thoracic aorta: what are the options? Eur J Cardiothorac Surg 35:77–82

Knoch M, Reul H, Kroger R, Rau G (1988) Model studies at mechanical aortic heart valve prostheses—part I: steady-state flow fields and pressure loss coefficients. J Biomech Eng 110:334–343

Kroll MH, Hellums JD, McIntire LV, Schafer AI, Moake JL (1996) Platelets and shear stress. Blood 88:1525–1541

Leverett L, Hellums J, Alfrey C, Lynch E (1972) Red blood cell damage by shear stress. Biophys J 12:257–273

Lim W, Chew Y, Chew T, Low H (1998) Steady flow dynamics of prosthetic aortic heart valves—a comparative evaluation with PIV techniques. J Biomech 31:411–421

Lissaman PBS (1983) Low-Reynolds-number airfoils. Annu Rev Fluid Mech 15:223–239

Liu JS, Lu PC, Chu SH (2000) Turbulence characteristics downstream of bileaflet aortic valve prostheses. J Biomech Eng 122:118–124

Paul R, Apel J, Klaus S, Schügner F, Schwindke P, Reul H (2003) Shear stress related blood damage in laminar couette flow. Artif Organs 27:517–529

Quinlan N, Dooley P (2007) Models of flow-induced loading on blood cells in laminar and turbulent flow, with application to cardiovascular device flow. Ann Biomed Eng 35:1347–1356

Raffel M, Willert CE, Kompenhans J (1998) Particle image velocimetry. Springer, Berlin

Schlichting H (1979) Boundary layer theory. McGraw-Hill, New York

Schoenhoff FS, Loupatatzis C, Immer FF, Stoupis C, Carrel TP, Eckstein FS (2009) The role of the sinuses of Valsalva in aortic root flow dynamics and aortic root surgery: evaluation by magnetic resonance imaging. J Heart Valve Dis 18:380–385

Sutera S, Joist T (1992) The haematological effects of non-physiological blood flow. In: Butchart E (ed) Thrombosis, embolism and bleeding, 1st edn. IRC Publishers, London, pp 149–159

Taira K, Colonius T (2009) Three-dimensional flows around low-aspect-ratio flat-plate wings at low Reynolds numbers. J Fluid Mech 623:187–207

Waite L, Fine JM (2007) Applied biofluid mechanics, 1st edn. McGraw-Hill, New York

Yagi T, Wakasa S, Tokunaga N, Akimoto Y, Akutsu T, Iwasaki K, Umezu M (2009) New challenge for studying flow-induced blood damage: macroscale modeling and microscale verification. In: Lim C, Goh C (eds) 13th international conference on biomedical engineering. Springer, Berlin, pp 1430–1433

Yarusevych S, Sullivan PE, Kawall JG (2006) Coherent structures in an airfoil boundary layer and wake at low Reynolds numbers. Phys Fluids 18:1–11

Yellin EL (1966) Laminar-turbulent transition process in pulsatile flow. Circ Res 19:791–804

Yoganathan AP, Corcoran W, Harrison E, Carl J (1978) The Bjork-Shiley aortic prosthesis: flow characteristics, thrombus formation and tissue overgrowth. Circulation 58:70–76

Yoganathan AP, Wick T, Reul H (1992) The influence of flow characteristics of prosthetic valves on thrombus formation. In: Buchart E (ed) Thrombosis, embolism and bleeding, 1st edn. IRC Publishers, London, pp 123–148

Zhao JB, Shi YB, Yeo TJ, Hwang NH (2001) Digital particle image velocimetry investigation of the pulsating flow around a simplified 2-D model of a bileaflet heart valve. J Heart Valve Dis 10:239–253